Catalysis Science & Technology

Accepted Manuscript

This article can be cited before page numbers have been issued, to do this please use: Z. Luo, J. Kong, Q. Bing, J. Liu and C. Zhao, *Catal. Sci. Technol.*, 2018, DOI: 10.1039/C8CY00037A.

This is an Accepted Manuscript, which has been through the Royal Society of Chemistry peer review process and has been accepted for publication.

Accepted Manuscripts are published online shortly after acceptance, before technical editing, formatting and proof reading. Using this free service, authors can make their results available to the community, in citable form, before we publish the edited article. We will replace this Accepted Manuscript with the edited and formatted Advance Article as soon as it is available.

You can find more information about Accepted Manuscripts in the author guidelines.

Please note that technical editing may introduce minor changes to the text and/or graphics, which may alter content. The journal's standard Terms & Conditions and the ethical guidelines, outlined in our author and reviewer resource centre, still apply. In no event shall the Royal Society of Chemistry be held responsible for any errors or omissions in this Accepted Manuscript or any consequences arising from the use of any information it contains.

ROYAL SOCIETY OF CHEMISTRY

rsc.li/catalysis

View Article Online
DOI: 10.1039/C8CY00037A

Catalysis Science & Technology

ARTICLE

Mechanism in Supported Ru_3Sn_7 Nanoclusters Catalyzed Selective Hydrogenation of Coconut Oil to Fatty Alcohols

Received 00th January 20xx,
Accepted 00th January 20xx

DOI: 10.1039/x0xx00000x

www.rsc.org/

Zhicheng Luo[1a], Qiming Bing[1b], Jiechen Kong[a], Jing-yao Liu[b*] and Chen Zhao[a*]

As a promising hydrotreating catalyst, it was previously reported that Ru…O=Sn (Ru electronically interacts with Sn oxides) on $RuSn/SiO_2$ was the active site for fatty acid hydrogenation, but here in this work we found that Ru_3Sn_7 nanoclusters on $RuSn/SiO_2$ were responsible for the selective hydrogenation of diverse fatty acids and coconut oil to fatty alcohols. The XPS results indicated no interaction between $Sn^{\delta+}$ and Ru^0, suggesting that SnO_x may exist as the isolated species. In contrary, the binding energy shifts of Ru^0 and Sn^0 at XPS spectra demonstrated a strong interaction, as a result from the formation of Ru_3Sn_7 alloy nanoclusters. It was demonsrated that the highest yield of fatty alcohol was obtained with a Sn/Ru ratio of 7/3 (hydrogenation rate: 2.45 $g{\cdot}g^{-1}{\cdot}h^{-1}$), and the careful selection of the Sn/Ru ratios and the reduction temperatures greatly suppressed the formation of Sn and SnO_2 phases. The ratio of stearyl alcohol formation rate to its consumption rate was 40.8 with Ru_3Sn_7/SiO_2 at selected conditions. In catalysts with a Sn/Ru ratio higher than 7/3, the presence of additional SnO_2 catalyzes the formation of undesired ester with a rate of 0.31 $g{\cdot}g^{-1}{\cdot}h^{-1}$. Excess SnO_2 would be reduced to Sn at temperatures higher than 600 °C, while Sn can catalyze ester by-product formation with a rate of 0.88 $g{\cdot}g^{-1}{\cdot}h^{-1}$. The DFT calculations showed that CH_3COOH adsorbs on the Ru_3Sn_7 (111) surface via Sn-O interactions at the two top sites of adjacent surface Sn atoms, and such adsortion was mainly due to the electrostatic interactions between the molecule and the positively charged surface Sn atoms. The charge density difference (CDD) plots of *co*-adsorbed CH_3CO^* and OH* intermediates indicated the bonding relationships of Sn-O and Ru-α-C, suggesting that the surface Sn atoms also took part in the catalytic reaction as an important surface sorption site as well as a Ru_3Sn_7 structure component, while Ru atoms bonded with α-C and hydrogenated the adsorbed intermediate species with the adsorbed H* to the final alcohol. Further indication that Ru_3Sn_7 were the active species in the bimetallic Ru-Sn catalyst was given by the much lower energy barrier for hydrogenation of acetic acid in Ru_3Sn_7 (111)(81.0 $kJ{\cdot}mol^{-1}$) compared to Ru (0001) (123.5 $kJ{\cdot}mol^{-1}$).

1. Introduction

The selective conversion of natural sources of oil to fatty alcohols holds increasing interest as a sustainable route for producing important intermediates used in the synthesis of cosmetics, surfactants, and plasticizers [1, 2]. The reaction pathway leading to the formation of fatty alcohols from triglycerides is displayed in Fig. S1. In order to form fatty alcohols from the hydrogenation of lipids with high selectivity and yield, three side-reactions need to be minimized: (1) the esterification between fatty acid intermediates and fatty alcohol products over acid or base sites; (2) the decarbonylation or hydrodeoxygenation of any aldehyde intermediates or alcohol products, respectively, to alkanes over metals such as Ni [3-5], Pd [6, 7], or Pt [8], sites; and (3) the dehydration of fatty alcohol products to olefins or ethers over acidic sites. The dissociation energy of the COO-R bond is particularly high at about 400 $kJ{\cdot}mol^{-1}$ [9], which indicates that the proper selection of a catalyst system with active sites that can efficiently activate inert COO-R bonds in triglycerides poses a particularly daunting challenge. In addition, the catalyst will need to operate at a temperature high enough to ensure high activity while simultaneously avoiding unwanted side reactions such as dehydration of fatty alcohols.

Great progress has been made in the field of homogeneous catalysis to achieve high yields of fatty alcohols from fatty esters. The catalysts include well-defined ruthenium complexes bearing chelating 2-(diphenylphosphino)-1-methylimidazole (PN) or pincer-type 2,6-(di-tert-butylphosphinomethyl)pyridine (PNP) ligands [10, 11]. More recently, non-noble-metal Fe pincer complexes have been reported to hydrogenate esters [12-14]. However, due to the high cost of the metal ligands used in these catalyst systems together with problems with respect to recycling the homogeneous catalysts, heterogeneous catalysts have proven to be more attractive choices for industrial applications. The

[a] Shanghai Key Laboratory of Green Chemistry and Chemical Processes, School of Chemistry and Molecular Engineering, East China Normal University, Shanghai, 200062, China
[b] Laboratory of Theoretical and Computational Chemistry, Institute of Theoretical Chemistry, Jilin University, Changchun, 130023, China.
1 Two authors contribute equally to the work
E-mail: czhao@chem.ecnu.edu.cn (C. Zhao)
Email: ljy121@jlu.edu.cn (J. Liu)
† Footnotes relating to the title and/or authors should appear here.
Electronic Supplementary Information (ESI) available: [details of any supplementary information available should be included here]. See DOI: 10.1039/x0xx00000x

View Article Online
DOI: 10.1039/C8CY00037A

well-known Cu-Cr based Adkins catalyst exhibits high efficiency for the hydrogenation of fatty esters to alcohols, but requires very harsh reaction conditions (250–350 °C and ca. 10–20 MPa H_2 pressure). In addition, toxicity problems associated with chromium compounds have driven researchers to find an efficient Cr-free catalyst. Thus bimetallic Cu-M catalysts such as Cu-Fe [15] and Cu-Zn [16, 17] have been developed for the formation of fatty alcohols derived from natural sources at high pressures. Recently, we reduced coconut oil to fatty alcohols with nearly 100% selectivity over a hydrothermally synthesized Cu/SiO_2 catalyst (consisting of surface $Cu_2O{\cdot}SiO_2$ and Cu^0 surface species) in methanol in absence of extraneous hydrogen [18]. In addition, other catalysts with noble metals [19-29] such as Rh, Ru, Pt, and Pd have been used to reduce ester derivatives. Among these, RuSn bimetallic catalysts are shown to very promising for the hydrogenation of esters or acids to alcohol [21,22]. It was recognized that the carbonyl of acid or acid derivatives (esters) polarized by either Sn^{2+} or Sn^{4+} Lewis acid sites can be hydrogenated by the H· radical transferred from an adjacent Ru-H site in a facile manner. Therefore, the interacted Ru…O=Sn species is generally considered as the active sites.

However, in this contribution, we report that the active sites for hydrogenation of fatty acids and fatty esters to fatty alcohols are demonstrated to be the supported Ru_3Sn_7 nanoclusters rather than Ru…SnO_2 (Ru electronically interacts with Sn oxides). The nature of the catalytic active sites was carefully explored by the detailed characterized and the relation with targeted catalytic tests. By comparing the formation energies and energy barriers of acid hydrogenation on potential facets, density function theory calculations reveal that the active sites are comprised of Ru_3Sn_7 nanoclusters. In addition, the role of Sn on RuSn for adsorption and reaction is explored by the charge density difference (CDD) plot.

2. Results and discussion

2.1 Catalyst screening for selective hydrogenation of stearic acid to stearyl alcohol

The rate-determining step in the conversion of triglycerides to fatty alcohols is the hydrogenation of fatty acids. [2] Therefore, a fatty acid (C_{18} stearic acid) was selected as the substrate for catalyst screening. A neutral SiO_2 support and a moderate hydrogenation temperature (240 °C) were used to minimize unwanted side-reactions such as dehydration of the target alcohol while maintaining appropriate catalyst activity. The noble metals Pt, Ru, and Pd, the non-noble metals Ni, Co, and Sn, and the bimetallic catalysts Ru-Pt, Pt-Sn, Pd-Sn, and Ru-Sn were incorporated into the SiO_2 support with a 5 wt% loading by incipient wetness impregnation. The XRD patterns of these catalysts are listed in Fig. S2.

To evaluate the activity of these catalysts, the hydrogenation of stearic acid was conducted in batch mode using dodecane as solvent, at conditions of 240 °C and 4 MPa H_2. As shown in Fig.1a, Almost all of the single metal catalysts (Pt, Ru, Ni, Co, and Sn) were inactive, except for Pd with a 30% conversion. Subsequently the bimetallic RuPt catalyst was tested, with the conversion of 20.6%. Whereas single Ru and Sn catalysts led to very small conversions (3% and 1.6%, respectively), we were gratified to find that there was a remarkable increase in the conversion up to 82.7% when the bimetallic $RuSn/SiO_2$ catalyst was employed, and the target product yield reached 80.0%.

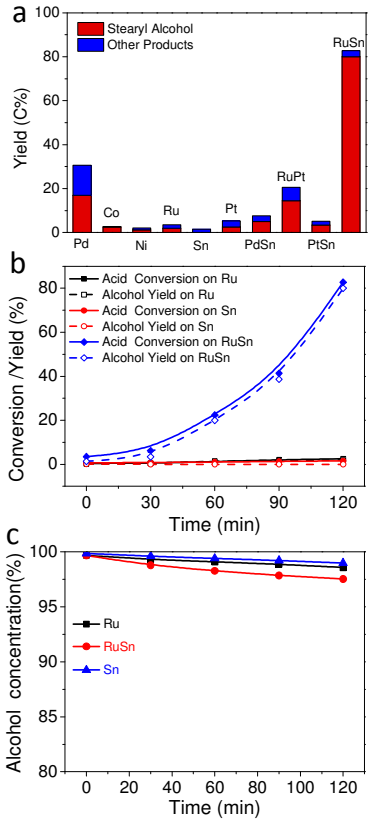

Fig. 1. (a) The product distributions for stearic acid hydrogenation over various metal centers supported on SiO_2. Reaction conditions: Stearic acid (1.0 g), catalyst (0.2 g, 5 wt.%), dodecane (80 mL), 240 °C, 4 MPa H_2, 120 min., and stirring at 700 rpm. (b) Stearic acid conversion and alcohols yield over various metal centers supported on SiO_2 as a function of time. Reaction conditions: Stearic acid (1.0 g), catalyst (0.2 g), dodecane (80 mL), 240 ˚C, 4 MPa H_2, stirring at 700 rpm. (c) The stability of stearyl alcohol over various metal centers supported on SiO_2 as a function of time. Reaction conditions: stearyl alcohol (1.0 g), catalyst (0.2 g), dodecane (80 mL), 240°C, 4 MPa H_2, stirring at 700 rpm.

Encouraged with this improvement in conversion with a noble metal-Sn bimetallic catalyst, PtSn and PdSn catalysts were also tested for stearic acid hydrogenation, but only led to poor substrate conversions (8.4%, and 7.5% conversion, respectively). As can be seen from the XRD patterns (Fig. S2), the bimetallic catalysts $PtSn/SiO_2$, $PdSn/SiO_2$, and $RuSn/SiO_2$ exhibited new diffraction peaks corresponding to $PtSn_4$ (JCPDS #65-9537), Pd_3Sn_2 (JCPDS #04-0801), and Ru_3Sn_7 (JCPDS # 26-0504), respectively, implying that the thermodynamically stable alloy phase was formed after co-impregnation of Sn and the corresponding noble metals. Those results indicate that

View Article Online
DOI: 10.1039/C8CY00037A
Catalysis Science & Technology ARTICLE

there is a synergistic interaction between Ru and Sn that plays a major role in improving the conversion of fatty acid hydrogenation. These results thus far suggested that in the highly active $RuSn/SiO_2$ catalyst, RuSn may form a new phase or that Sn in the form of the oxide (SnO_2) could dramatically modify the metallic Ru center.

The kinetics curves of stearic acid hydrogenation for the tested catalysts, showed that RuSn achieved the highest hydrogenation rate (2.02 $g{\cdot}g^{-1}{\cdot}h^{-1}$), while such hydrogenation rates were 0 with Sn sites and 0.07 $g{\cdot}g^{-1}{\cdot}h^{-1}$ with Ru sites (Fig. 1b). The comparative kinetics curves on other metals (Pt, Ru, Ni, Co, RuPt, PtSn, and PdSn) were displayed in Fig. S3. In addition, the stability of the produced fatty alcohol with the developed RuSn catalysts at selected conditions should also be considered. As displayed in Fig. 1c, the conversion rate of stearyl alcohol over $RuSn/SiO_2$ was 0.06 $g{\cdot}g^{-1}{\cdot}h^{-1}$, while such rates were 0.04 and 0.02 $g{\cdot}g^{-1}{\cdot}h^{-1}$ over Ru/SiO_2 and Sn/SiO_2, respectively. Thus, the ratio of stearyl alcohol formation rate to consumption rate was 40.8 with $RuSn/SiO_2$ at 240 °C, indicating that the target product was relatively stable at selected catalytic conditions, as shown in Table 1. Having ascertained the optimal catalyst for the model reaction involving stearic acid hydrogenation, we next sought to further understand and explore the nature of the active site through catalytic tests and a detailed characterization of the $RuSn/SiO_2$ catalyst.

Table 1. Calculated reaction rates over different catalysts.

Catalyst	Ru/SiO_2	Sn/SiO_2	$RuSn/SiO_2$
Alcohol formation rate ($g{\cdot}g^{-1}{\cdot}h^{-1}$)	0.07	0	1.98
Alcohol consumption rate ($g{\cdot}g^{-1}{\cdot}h^{-1}$)	0.04	0.02	0.06

2.2 Characterization of Ru_xSn_y/SiO_2 samples

In order to modify the Sn/Ru ratio in the $RuSn/SiO_2$ catalysts, the Ru content was kept constant at 1.5 wt.%, while the Sn content varied from 0 to 9.0 wt.%. The XRD spectra of the resulting catalysts were recorded in order to observe phase transformations as the Sn/Ru ratio was varied (Fig. 2). The monometallic Ru/SiO_2 catalyst displayed the typical main peaks observed in hexagonal crystalline Ru (JCPDS #65-1863), with (100), (002), (101), and (102) reflection planes present. When 1.5 wt.% Sn was incorporated, the peak intensity corresponding to Ru became weaker, while a new peak corresponding to Ru_3Sn_7 (JCPDS # 26-0504) appeared. As the Sn content was increased to 4.5 wt.%, the Ru characteristic peak disappeared and the peak of Ru_3Sn_7 was observed. The peak intensity corresponding to cubic Ru_3Sn_7 gradually increased up to 9 wt.%. It should be noted that an additional SnO_2 species (JCPDS # 41-1445) was observed in the XRD patterns as higher amounts of Sn were incorporated into the catalyst.

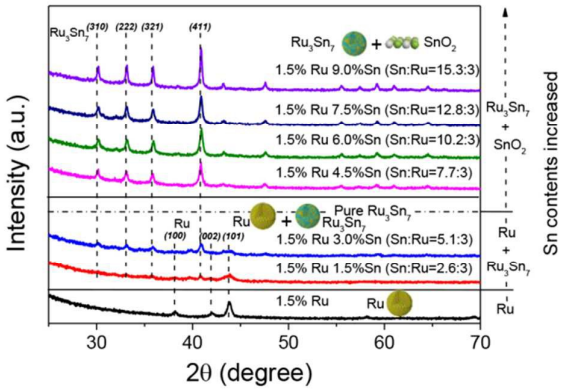

Fig. 2. The XRD patterns of Ru/SiO_2 and $Ru\text{-}Sn/SiO_2$ samples with different ratios of Sn to Ru.

The TPR-H_2 profiles of calcined metallic catalysts help to identify the surface species during the hydrogen reduction process (Fig. 3). Therefore, we conducted TPR-H_2 experiments on the hydrogenation of calcined single metal catalysts (Sn, Ru), and the bimetallic Ru-Sn catalyst with Sn/Ru ratios varying from 2.6/3 to 15.3/3 (i.e. corresponding to Sn/Ru wt.% ratios ranging from 1.5/1.5 to 9/1.5). In the 5 wt.% monometallic Sn catalyst, SnO_2 was reduced at around 645°C, while in the single 1.5 wt.% Ru catalyst, RuO_2 was reduced at around 150 °C. In the 1.5 wt.% Ru-1.5 wt.% Sn catalyst, the RuO_2 reduction peak became broader, indicating a shift in the reduction temperature of RuO_2 that is closer to SnO_2 due to interactions between RuO_2 and SnO_2. In the 1.5 wt.% Ru-4.5 wt.% Sn bimetallic RuSn catalyst (corresponding to a Sn/Ru atomic ratio of 7.7/3, higher than the Sn/Ru ratio in the Ru_3Sn_7 nanocluster), the SnO_2 reduction peak at around 645 °C disappeared, and a new broad peak for SnO_2 reduction appeared at 515 °C. The lowered reduction temperature is probably due to weak interactions between isolated SnO_2 and RuO_2 species on the SiO_2 support surface. Moreover, an additional peak emerged at around the reduction temperature ranges of 350-460 °C, probably corresponding to the reduction of SnO_2 species that is close to RuO_2. Hence, 460 °C is the minimum temperature requirement for fully reduced Sn to incorporate with Ru atoms, thereby forming Ru_3Sn_7 nanoclusters.

To prove our hypothesis regarding the temperature requirements for the reduction of SnO_2 to form Ru_3Sn_7 nanoclusters, we obtained the XRD patterns of the catalyst samples after reducing calcined 1.5 wt.% Ru-4.5 wt.% Sn/SiO_2 under a continuously flowing H_2 atmosphere at 250 °C, 460°C, and 600 °C. As can be seen from the XRD patterns (Fig. S4), the SnO_2 peak (JCPDS # 41-1445) was still detected after conducting the hydrogenation at 250 °C, showing that SnO_2 reduction had not taken place. It should be observed that in XRD experiments the Ru^0 peak is not observable when the Ru particles are too small. When the reduction temperature was increased to 460 °C, the characteristic XRD peaks corresponding to Ru_3Sn_7 (JCPDS # 26-0504) appeared, demonstrating that the reduction peak at 400 °C close to the RuO_2 peak (150 °C) in the TPR-H_2 profile corresponded to the

View Article Online
DOI: 10.1039/C8CY00037A

reduction temperature of SnO_2 species. At higher temperatures no additional XRD peaks are observed; in addition, the intensity of the Ru_3Sn_7 peak increases as increasing amounts of reduced Ru and Sn species associate to form the nanoclusters.

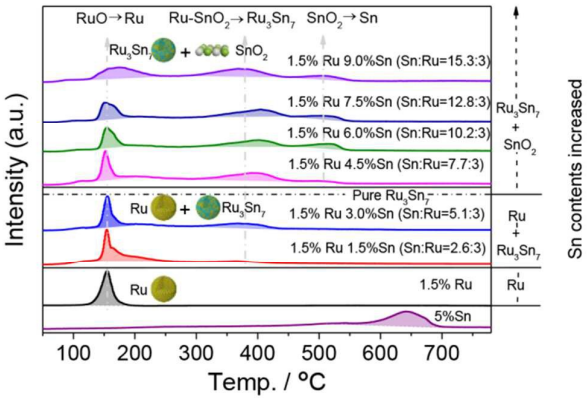

Fig. 3. The temperature-programmed hydrogen reduction of calcined Ru/SiO_2, Sn/SiO_2, and $RuSn/SiO_2$ samples with varying Ru/Sn ratios.

Subsequently, FT-IR spectra of Ru/SiO_2 and Ru_xSn_y/SiO_2 samples with adsorbed CO were taken to provide further insights on the nature of the surface composition (Fig. 4). The IR spectrum of the Ru/SiO_2 sample showed three main peaks: a low intensity band at 2134 cm^{-1}, a very intense one at 2078 cm^{-1}, and a broad unsymmetrical band at 2016 cm^{-1}, assigned to the $Ru^{\delta+}$-$(CO)_x$, $Ru^{\delta+}$-$(CO)_2$, and Ru^0-CO absorption bands [30, 31],respectively. As Sn was added to Ru (Sn/Ru ratio < 7/3) thus forming Ru-Sn bimetallic catalysts, the intensity of the CO adsorption peak sharply decreased, indicating that Ru-Sn alloyed nanoclusters began to form and that such nanoclusters inhibited CO adsorption on the surface. When the Sn/Ru ratio exceeded 7/3, and the main species present were Ru_3Sn_7 and SnO_2, CO adsorption on the Ru-Sn catalysts completely disappeared.

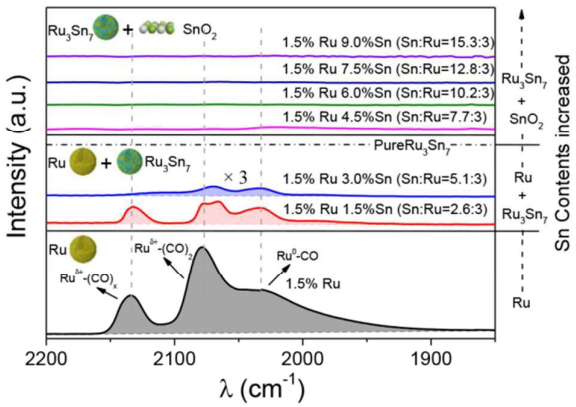

Fig. 4. The infrared spectra of adsorbed CO on $RuSn/SiO_2$ samples with varying Ru/Sn ratios.

The XPS technique is conducted to obtain valuable information of surface species on the catalysts. The binding energy (BE) of Ru $3d_{5/2}$ and Sn $3d_{5/2}$ in the reduced $RuSn/SiO_2$ are summarized in Table S1 and Fig. 5. The reduced Ru/SiO_2 catalyst showed a Ru 3d5/2 peak at 280.2 eV, corresponding to the Ru^0 species, as shown in Fig. 5a. The reduced Sn/SiO_2 catalyst demonstrated a wide Sn $3d_{5/2}$ peak centered at 486.9 eV and a weak shoulder at 484.9 eV, which were oxidized tin species ($Sn^{\delta+}$), and reduced tin species (Sn^0), respectively, as displayed in Fig. 5b. However, the XPS technique cannot distinguish Sn^{2+} and Sn^{4+} species due to the similar BE values. On the reduced $Ru\text{-}Sn/SiO_2$ catalysts with increased Sn loadings (0, 1.5, 3.0, to 4.5 wt%), the BE of Ru^0 $3d_{5/2}$ was dramatically decreased from 280.2, 279.8, 279.7 to 279.4 eV, suggesting the state of Ru was largely altered, perhaps due to the formation of Ru_3Sn_7 alloy. Till the addition of 4.5 to 9.0 wt% Sn, the BE values of Ru became almost stable at ca. 279.2 eV, attributed to the equilibrium of Ru and Sn atoms in the Ru_3Sn_7 alloy. While, the BE of Sn^0 $3d_{5/2}$ increased from 484.9 to 485.3 with the increase of Ru/Sn ratio. The decreased BE of Ru^0 and the increased BE of Sn^0 indicated an electron transfer from Ru^0 to Sn^0, further suggesting the formation of RuSn alloys. However, the BE of $Sn^{\delta+}$ kept unchanged at 486.9 eV on those RuSn samples, suggesting the isolated species and no interactions between $Sn^{\delta+}$ and Ru^0. Hence, these results directly demonstrate the interaction between Ru^0 and Sn^0 rather than between Ru^0 and $Sn^{\delta+}$. In addition, the surface atomic ratios of $Sn^0/Sn^{\delta+}$ on $Ru\text{-}Sn/SiO_2$ reached the maximum value at 0.8 with a Sn content of 4.5 wt% (see Table S1), demonstrating the most abundant Ru_3Sn_7 clusters at such Ru/Sn ratio. With the increasing Sn contents (higher than 4.5 wt%), isolated SnO_2 began to form. Such SnO_2 species had no electron transfer with Ru^0, suggested from the stable BE values of $Sn^{\delta+}$ XPS at 486.9 eV. The results gained from XPS spectra are highly consistent with the XRD, TPR-H_2, IR-CO results in the former part.

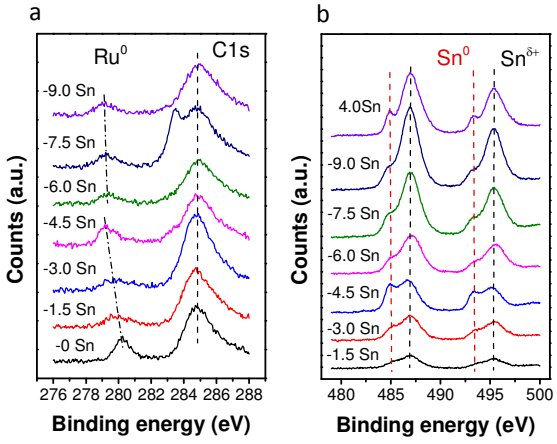

Fig. 5. XPS spectra of $RuSn/SiO_2$ samples with varying Ru/Sn ratios. (a) Ru $3d_{5/2}$; (b) Sn $3d_{5/2}$. The Ru content was constant at 1.5 wt.%, while the Sn content varied from 0 to 9.5 wt.%.

Based on the results from the XRD, TPR-H_2, IR-CO and XPS experiments of the Ru, Sn, and Ru-Sn catalysts, some general conclusions can be reached. After reduction of a catalyst with

View Article Online
DOI: 10.1039/C8CY00037A

a Sn/Ru ratio lower than 7/3, the main species present are Ru^0 and Ru_3Sn_7 nanoclusters, while further increasing the Sn/Ru ratio leads to Ru_3Sn_7 and SnO_2 being mainly formed. SiO_2 supported single metal Ru and Sn catalysts have substrate conversion of only 5% and 1.6% respectively, and thus single Ru and Sn metal centres can be excluded as significant active sites. Therefore, the most active catalytic sites should comprise Ru-Sn bimetallic centres, with the Ru-SnO_2, Ru_3Sn_7, and Ru_3Sn_7-SnO_2 species being likely candidates as the most significant active sites.

2.3 Understanding the nature of active sites on RuSn/SiO_2 catalyst for hydrogenation of fatty acids

To further elucidate the active sites which are responsible for fatty acid hydrogenation, we first used SiO_2 and the SnO_2/SiO_2 catalyst to investigate the effectiveness of the support and the catalyst towards the esterification side reaction between the target product fatty alcohol and the reactant fatty acid. The kinetics for the reaction was recorded in dodecane at 240°C in the presence of H_2 at 4 MPa pressure (Fig. 6a and 6b). Whereas SiO_2 was almost completely inert towards ester formation, only attaining 2% conversion after 120 min, SnO_2/SiO_2 led to a relatively fast reaction with a rate of 0.31 $g{\cdot}g^{-1}{\cdot}h^{-1}$, and after 120 min ester was formed with 12.3% conversion, implying that silica supported SnO_2 can promote the formation of the ester side product.

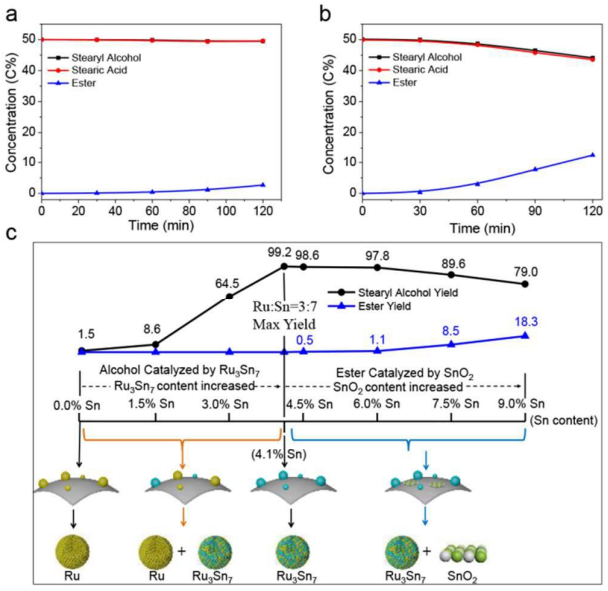

Fig. 6. Product distributions of conversion of stearic acid and stearyl alcohol on the catalysts (a) SiO_2, and (b) 5 wt.% SnO_2/SiO_2. Reaction conditions: stearic acid (0.5 g), stearyl alcohol (0.5 g), catalyst (0.2 g), dodecane (80 mL), 240°C, 4 MPa H_2, 0-120 min, stirring at 700 rpm. (c) Impact of Sn/Ru ratios towards product distributions from stearic acid conversion. Reaction conditions: Stearic acid (1.0 g), RuSn/SiO_2 (0.2 g, Ru loading: 1.5 wt%, Sn loading: 0-9 wt%), dodecane (80 mL), 240 °C, 4 MPa H_2, 120 min, stirring at 700 rpm.

Secondly, the Sn/Ru atomic ratio was varied and was found to have a dramatic effect on the product distributions, as shown in Fig 6c. With the monometallic 1.5 wt.% Ru/SiO_2 catalyst, a conversion of only 1.6% was achieved, indicating that single Ru^0 metallic centres are nearly inactive under the selected conditions. In the bimetallic catalyst, as the Sn content increased from 1.5 wt.% to 3.0 wt.%, the yield for fatty alcohol formation sharply increased from 8.6% to 64.5%, respectively. Within these Sn content ranges, the main catalytic species in the reduced samples are Ru and Ru_3Sn_7. The highest yield of fatty alcohol (99.2%) was achieved when the Sn wt.% was 4.1%, corresponding to the formation of Ru_3Sn_7 species. With greater Sn contents (4.5 to 9.0 wt.% Sn, i.e. Sn/Ru ratios greater than 7/3), the yield of fatty alcohol decreased (from 98.2% to 79.0%), and the yield of the ester side-product increased (from 0.5% to 18.3%) as a result of additional SnO_2 formation as shown from the TPR-H_2 experiment. These results strongly suggest that the most active catalytic sites for alcohol formation are Ru_3Sn_7 nanoclusters, while SnO_2 species are responsible for catalyzing the esterification of fatty alcohols and acids. Therefore, the optimal catalyst for fatty alcohol formation is achieved with a Sn/Ru ratio of 7/3. In catalysts with a Sn/Ru atomic ratio < 7/3, the alcohol yields increase with larger amounts of Sn up to a ratio of 7/3, while a Sn/Ru atomic ratio > 7/3 led to the SnO_2 catalyzed formation of ester by-product.

Apart from the effect of the Sn/Ru ratios, which determines the type of catalytic species present, the reduction and the oxidation state of the Ru and Sn species has a significant effect on the product distribution obtained from fatty acid hydrogenation (Fig. S4). For example, as shown in Fig. 7a, with a reduced Sn/SiO_2 catalyst the esterifcation of stearic acid and stearyl alcohol took place with a rate of 0.88 $g{\cdot}g^{-1}{\cdot}h^{-1}$, which was much greater than that with the SnO_2/SiO_2 catalyst (Fig. 6b). With the calcined 1.5 wt.% Ru-4.5 wt.% Sn/SiO_2 catalyst (corresponding to a Sn/Ru ratio slightly higher than 7/3) at 25°C, the target alcohol was obtained in 17.3% yield (Fig. 7b). In this case, the main species are inferred to be Ru·SnO_2 and SnO_2 which are inactive for substrate hydrogenation, but which would be reduced in-situ by the hydrogen present in the catalytic reduction to metallic Ru^0 at 240 °C. With the same catalyst, at 250°C stearyl alcohol was obtained in only 47% yield. At this temperature, the main surface species were Ru·SnO_2 and SnO_2. The maximum yield of stearyl alcohol was nearly quantitative (98.6%), and was achieved at a reduction temperature of 460 °C. This result further implied that the catalytic species was Ru_3Sn_7 (the main species present after reduction at 460°C), but not Ru…O=Sn (Ru electronically interacts with Sn oxides). At 600 °C, the presence of trace quantities of Sn in addition to the main Ru_3Sn_7 species led to a lower fatty alcohol yield (87.8%) and a higher yield of ester by-product (6.7%). These results show how the composition of the RuSn catalyst changes with varying Sn/Ru ratios (Fig. 6c) and reduction temperatures (Fig. 7b). With the monometallic Ru catalyst and reduction at 460°C, Ru nanoclusters were dispersed on the SiO_2 support surface. At the same temperature, when the tin content was increased to 1.5 or 3.0 wt.% (corresponding to a Sn/Ru ratio < 7/3), SnO_2 species were reduced to Sn, which then associated with free

View Article Online
DOI: 10.1039/C8CY00037A

Ru^0 sites to form Ru_3Sn_7 nanoclusters. Therefore, when the Sn/Ru ratio is lower than the coordination number, isolated SnO_2 species are not present. When the Sn wt.% matches the Sn/Ru ratio of 7/3, Ru_3Sn_7 nanoclusters are exclusively formed on the surface of SiO_2. As the Sn content further increases (4.5–9.0 wt.%), unreduced SnO_2 species were present along with the Ru_3Sn_7 nanoclusters.

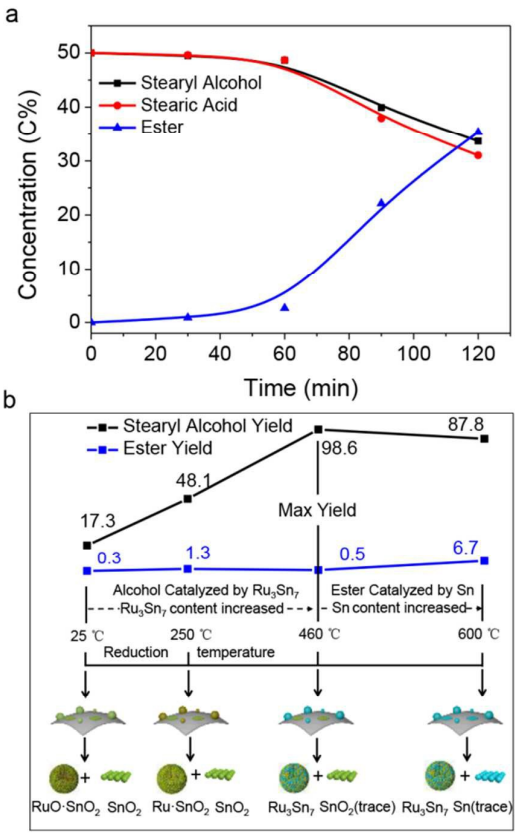

Fig. 7. (a) The product distributions reacted with stearic acid and stearyl alcohol on 5 wt.% Sn/SiO_2 as a function of time. Reaction conditions: stearic acid (0.5 g), stearyl alcohol (0.5 g), Sn/SiO_2 (0.2 g), dodecane (80 mL), 240°C, 4 MPa H_2, stirring at 700 rpm. (b) Impact of the reduction temperatures of Ru-Sn/SiO_2 samples towards product distributions from stearic acid conversion. Reaction conditions: stearic acid (1.0 g), 1.5%Ru 4.5%Sn/SiO_2 (0.2 g), dodecane (80 mL), 240°C, 4 MPa H_2, 120 min., stirring at 700 rpm.

Our results strongly indicate that the active sites for hydrogenation are Ru_3Sn_7 nanoclusters, while Sn or SnO_2 species present when the Sn wt.% > 4.1 can both catalyze the formation of ester side product. However, it was previously reported that non-alloyed Ru…O=Sn species (… represents that Ru electronically interacts with Sn oxides) dispersed on the catalyst support surface, rather than a Ru-Sn alloy as suggested by our findings was the active site for acid hydrogenation. The carbonyl of acid or acid derivatives (esters) can be polarized by either Sn^{2+} or Sn^{4+} Lewis acid sites [32, 33], and the activated carbonyl carbon can then be hydrogenated by a H· radical transferred from an adjacent Ru-H site. While the electronic interaction of tin with an adjacent ruthenium is thought to poison the active site responsible for hydrogen activation, Pouilloux et al. pointed out the existence two tin oxide species (SnO_x and SnO_y), where the SnO_x species (x<y) would interact closely with ruthenium without significant formation of Ru_nSn_m alloy [34]. These SnO_x species interact with the C=O bond of the ester to promote transfer of activated hydrogen bound to ruthenium to receive an acetal of tin. Such acetal is subsequently converted to an aldehyde, which is then fast hydrogenated into the final alcohol. In addition, excessive SnO_y can block free Ru^0 sites, suppressing the hydrogenation capability (see Scheme 1a).

Based on our results, we suggest that non-alloyed Ru…Sn=O species are not the active sites for acid hydrogenation. First, the highest fatty alcohol yield was obtained when the predominant surface species were Ru_3Sn_7 nanoclusters (Fig. 6c). If Ru…Sn=O was the active catalyst, the highest activity should be reached when the Sn content is higher than 4.1%, which corresponds to catalysts where free tin and tin oxides are present. Secondly, the XRD patterns and TPR-H_2 profiles demonstrate that in hydrogenation conducted with the 1.5 wt.% Ru-4.5 wt.% Sn/SiO_2 catalyst the main species present at 250 °C, 460 °C, and 600 °C were Ru-SnO_2, Ru_3Sn_7 and trace amounts of SnO_2, and Ru_3Sn_7-Sn respectively. However, the highest yield was achieved at a reduction temperature of 460 °C, where Ru_3Sn_7 species are predominantly present. Third, XPS results did not indicate interaction between $Sn^{\delta+}$ and Ru^0 due to the unchanged BE vaules of $Sn^{\delta+}$, suggesting that SnO_x may exist as the isolated species. In contrary, the BE shifts on Ru^0 and Sn^0 in XPS spectra indicated a strong interaction due to the formation of Ru_3Sn_7 nanoclusters. Hence, Ru_3Sn_7 nanoclusters, rather than Ru…Sn=O species are concluded to be the principal catalytic sites. We deduce that, in our case, the oxygen in the carbonyl group prefers to be adsorbed on Sn atoms of Ru_3Sn_7/SiO_2 clusters, which would be easily attacked by a H· bound to Ru. This species would be sequentially hydrogenated to an aldehyde intermediate, and eventually to the target fatty alcohol product (see Scheme 1b).

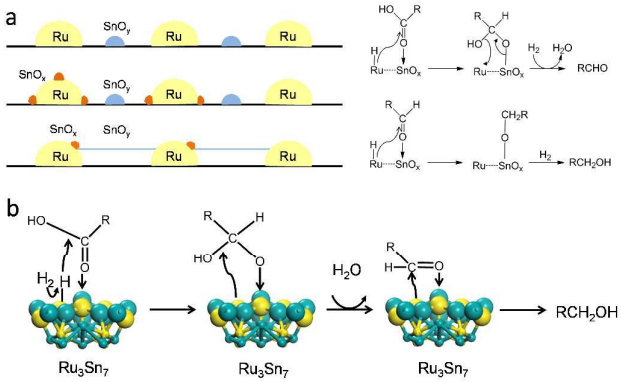

Scheme 1. Mechanism of the hydrogenation of ester into alcohol over RuSn catalyst (a) presented by Pouilloux, (b) presented by ours. Color scheme: yellow: Ru; cyan: Sn.

View Article Online
DOI: 10.1039/C8CY00037A

Subsequently, a detailed characterization was performed on the most active $RuSn/SiO_2$ catalyst, with a Ru/Sn atomic ratio of 7 to 3. The optimized catalyst achieved the hydrogenation of stearic acid to the corresponding fatty alcohol in 99.2% yield (see Fig. 6c). The BET surface area of $Ru-Sn/SiO_2$ was 177 $m^2 \cdot g^{-1}$ (Fig. 8a), while the XRD patterns showed that the main catalytic sites were Ru_3Sn_7 nanoclusters (Fig. 8b). The TEM image of the Ru_3Sn_7 nanoclusters on the amorphous SiO_2 support showed that the particles were small at around 3.9 ± 1.3 nm (Fig. 8c). In addition, TEM-mapping of a selected portion of the TEM image demonstrated that the Ru_3Sn_7 nanoclusters were dispersed throughout the support surface (Fig. 8d).

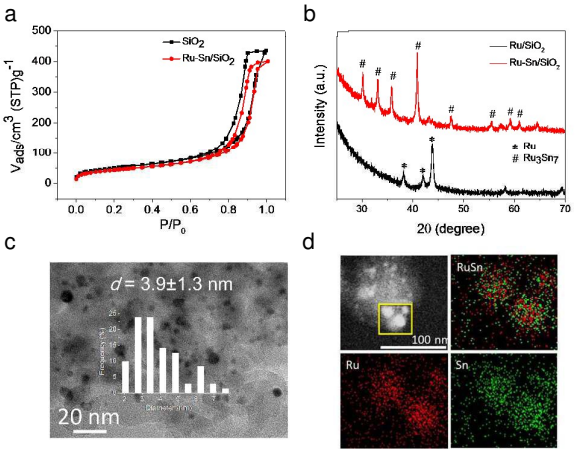

Fig. 8. Characterization of $Ru-Sn/SiO_2$ catalyst by (a) N_2 adsorption and desorption isotherms, (b) XRD pattern, (c) TEM, and (d) TEM-Mapping.

2.4 The extension of the substrate and coconut oil hydrogenation to fatty alcohols

Having ascertained the composition of the most active catalyst (Ru_3Sn_7), we explored the effect of hydrogen pressure (ranging from 2 to 4 MPa) towards product selectivity (Fig S5a). We were gratified to find that on increasing the pressure from 2 to 4 MPa, the selectivity increased from 48.9% to 99.2%, suggesting that relatively high hydrogen pressures favor the equilibrium for octadecanal hydrogenation to the side of reduced product, i.e., stearyl alcohol. As the H_2 pressure increased up to 5 MPa, the selectivity towards stearyl alcohol was nearly constant at 100%. Then, we investigated the influence of temperature (from 220-280 °C) on the hydrogenation of stearic acid under identical conditions (Fig. S5b). The reaction rates increased from 1.74 to 4.51 $g \cdot g^{-1} \cdot h^{-1}$ within the 220–280 °C tested temperature range, representing in the apparent activation energy of 36 $kJ \cdot mol^{-1}$ (Fig. S5c). Therefore, 240°C and 4 MPa H_2 were selected as the optimal temperature and hydrogen pressure for the best catalytic performance.

Having developed a catalyst system for the efficient reduction of stearic acid to the corresponding fatty alcohol, the reduction of a series of C_{12}-C_{18} fatty acids (lauric acid, myristic acid, palmitic acid, and stearic acid) was carried out with Ru_3Sn_7/SiO_2 and the optimized reduction conditions (dodecane as solvent, 240°C, 4 MPa H_2), with the results in Table 2. The selectivity for fatty alcohols and the conversion were nearly 100%, with hydrogenation rates varying from 2.47 $g \cdot g^{-1} \cdot h^{-1}$ (palmitic acid) to 4.85 $g \cdot g^{-1} \cdot h^{-1}$ (myristic acid). For the hydrogenation of C_3 propionic acid and C_4 butyric acid, lower conversions of 84.2% and 81.3% together with selectivity of 83.5% and 80.4%, respectively were attained. However, the apparently lower activity of the catalyst on C_3 and C_4 acids may be due to the lower solubility of these reactants in dodecane.

Table 2. Hydrogenation of C_3-C_{18} acid and coconut oil to the corresponding alcohols catalyzed by Ru_3Sn_7/SiO_2

Substrate	Conv. (C%)	Selectivity (%)			Rate ($g \cdot g^{-1} \cdot h^{-1}$)
		Alcohol	Alkane	Ester	
Propionic acid	84.2	83.5	0.50	0.21	2.10
Butyric acid	81.3	80.4	0.38	0.47	2.03
Lauric acid	99.2	98.5	0.63	0.86	2.59
Myristic acid	99.3	99.6	0.36	0.09	4.85
Palmitic acid	99.0	99.7	0.23	0.12	2.47
Stearic acid	100	99.0	0.55	0.49	2.45
Coconut oil	99.5	96.6	3.03	0.38	0.79

Reaction conditions: substrate (1.0 g), Ru_3Sn_7/SiO_2 catalyst (0.2 g), dodecane (80 mL), 240 ˚C, 4 MPa H_2, 120-240 min., stirring at 700 rpm.

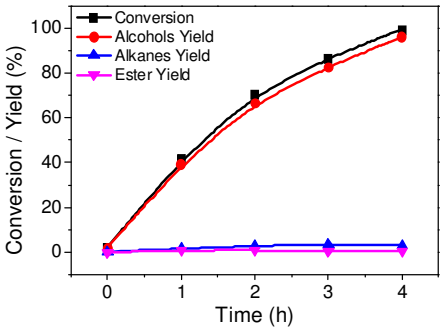

Fig. 9. Kinetics of coconut oil conversion over Ru_3Sn_7/SiO_2 catalyst. Reaction conditions: coconut oil (1.0 g), Ru_3Sn_7/SiO_2 (0.2 g, Ru loading: 1.5 wt%, Sn loading: 4.1 wt%), dodecane (80 mL), 240°C, 4 MPa H_2, stirring at 700 rpm.

Finally, the optimized catalyst and reaction conditions were employed for the hydrogenation of coconut oil (Fig. 9), which took place with nearly 100% conversion and selectivities of 96.6% C_8-C_{18} fatty alcohol, 3% C_8-C_{18} alkane and 0.4% heavier ester in 240 min. The gained fatty alcohol formation rate was 0.79 $g \cdot g^{-1} \cdot h^{-1}$. The fatty alcohol composition closely

View Article Online
DOI: 10.1039/C8CY00037A

mirrored the fatty acid composition of raw coconut oil (for a detailed composition analysis, see Fig. S6), with the major components being C_{12} lauryl alcohol (49.7%) and C_{14} myristyl alcohol (18.0%). The alkanes that were obtained originated from hydrodeoxygenation of fatty alcohols.

In addition, the stability on Ru_3Sn_7/SiO_2 catalyst for coconut oil hydrogenation was tested by four consecutive runs, which attained stable activities and selectivity (Fig. S7). The reused catalysts after four runs were subsequently characterized by TEM, XRD, and XPS measurements. The TEM images and XRD patterns (Fig. S8 and Fig. S9) showed that Ru_3Sn_7/SiO_2 was only slightly sintered with the particle size of ca. 5 nm after four consecutive runs. The comparable XPS spectra before and after recycling runs demonstrated that the Ru and Sn states on Ru_3Sn_7/SiO_2 catalyst were almost not changed (Fig. S10). A highly durable of Ru_3Sn_7/SiO_2 catalyst is thus demonstrated.

2.5 DFT calculations

First-principles density functional theory (DFT) calculations were carried out to gain deeper insights into the structure of the active catalyst and the mechanism for the catalytic hydrogenation reaction with the RuSn bimetallic catalyst (see SI for further computational details). First, to elucidate the reason for the formation of Ru_3Sn_7 species as the major alloy in the RuSn catalyst, even when the Sn content used during preparation of the catalyst led to a Ru/Sn ratio different from 3/7 (see Fig. 6c), we calculated the formation energy of the three possible RuSn alloy (Ru_1Sn_2, Ru_2Sn_3 and Ru_3Sn_7) from which crystal structure data are available [35, 36]. The DFT calculations showed that the Ru_3Sn_7 alloys had the lowest formation energy at −21.2 kJ·mol^{-1}·atom^{-1}, compared with −15.4 kJ·mol^{-1}·atom^{-1} and −18.3 kJ·mol^{-1}·atom^{-1} for the Ru_1Sn_2, and Ru_2Sn_3 alloys respectively, thus leading Ru_3Sn_7 to be preferentially formed in the RuSn bimetallic catalyst, which is entirely consistent with our experimental observations. The negative formation energies of the three alloys also indicate that the Ru and Sn metal components preferentially combine to form RuSn alloys rather than remain as separate metals during the preparation of RuSn catalyst.

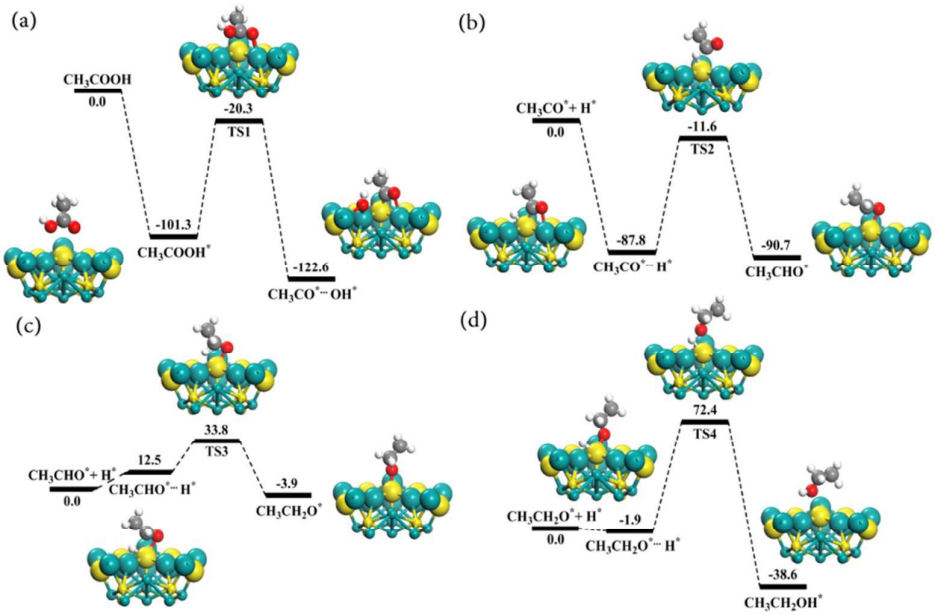

Fig. 10. Potential energy diagrams and optimized geometries of all reaction intermediates and transition states for different steps (a–d) in the catalytic hydrogenation reaction of acetic acid to ethanol on Ru_3Sn_7 (111) surface. Energies (kJ·mol^{-1}) include zero-point-energy correction. Only the upper two layers of Ru_3Sn_7 (111) surface are shown in the diagrams. Color scheme: yellow: Ru; cyan: Sn, grey: C, red: O, and white: H.

Table 3. Calculated reaction energies (ΔH), energy barriers (E_a) and interaction energies between coadsorbates for different steps in the hydrogenation of acetic acid to ethanol on Ru_3Sn_7 (111) surface.

Step	Reaction	ΔH (kJ/mol)	E_a (kJ/mol)	E_{inter} (kJ/mol)
1	$CH_3COOH + {}^* \rightarrow CH_3COOH^*$	-101.3	/	/
2	$CH_3COOH^* \rightarrow CH_3CO^* + OH^*$	-21.3	81.0	/
3	$CH_3CO^* + H^* \rightarrow CH_3CHO^*$	-2.9	76.2	-87.8
4	$CH_3CHO^* + H^* \rightarrow CH_3CH_2O^*$	-16.4	21.3	12.5
5	$CH_3CH_2O^* + H^* \rightarrow CH_3CH_2OH^*$	-36.7	74.3	-1.9

To understand the source of the high reaction activity of the RuSn alloy, the mechanism of the hydrogenation reaction on Ru_3Sn_7 (111) surface, which is the major crystal surface determined by the experiment in this work, was studied by DFT calculations and compared with that on Ru(0001) (the surface structures are shown in Fig. S11).[37] To simplify the calculations, a model reaction based on the simpler but analogous reactant acetic acid (CH_3COOH) was studied. The intermediates present during the hydrogenation of CH_3COOH to ethanol (CH_3CH_2OH) on the Ru_3Sn_7 (111) surface are shown in Fig. 10. In the first step, CH_3COOH adsorbs on the Ru_3Sn_7

View Article Online
DOI: 10.1039/C8CY00037A

(111) surface via Sn-O interactions at the two top sites of adjacent surface Sn atoms, with an adsorption energy of −101.3 kJ·mol^{-1} and the average Sn-O distance of 3.62 Å. According to the Bader electron analysis results, on the Ru_3Sn_7 (111) surface, Ru atoms possess negative charge of – 0.64 |e| in average, while Sn atoms have positive charge of +0.34 |e| in average. Thus, the adsorption of CH_3COOH molecule to the Ru_3Sn_7 (111) surface is mainly due to the electrostatic interactions between the molecule and the positively charged surface Sn atoms. The reduction of CH_3COOH* begins with the breaking of the carbonyl carbon-hydroxyl oxygen (C-O) bond, with an energy barrier of 81.0 kJ·mol^{-1}, yielding adsorbed CH_3CO* and OH* intermediates. The CH_3CO* species adsorbs on the Ru_3Sn_7 (111) surface with the Sn-O and Ru-C bond lengths of 2.30 and 1.99 Å, respectively, while the OH* species adsorbs at the bridge site between two surface-Sn atoms with an average Sn-O bond length of 2.32 Å. Then, the intermediate Sn-bound CH_3CO* species undergoes a three-step successive hydrogenation process to form the final ethanol product involving two hydrogenated intermediates of CH_3CHO* and CH_3CH_2O*. Our calculations of the adsorption of H* species on Ru_3Sn_7 (111) surface suggest that H* prefers to adsorb on the Ru atom than the Sn atom (Figure S12), indicating that the hydrogenation reaction is more likely to happen on the Ru atom site. The first step involves hydrogen transfer to the acyl radical intermediate ($CH_3CO^{\cdots}H$) followed by transfer to the corresponding aldehyde ($CH_3CHO^{\cdots}H$), yielding an ethoxy radical which abstracts a third equivalent of hydrogen ($CH_3CH_2O^{\cdots}H$). The energy barriers for these three steps are 76.2 kJ·mol^{-1}, 21.3 kJ·mol^{-1}, and 74.3 kJ·mol^{-1} (Table 3), respectively. The resulting CH_3CH_2OH is adsorbed above a layer of Ru atoms.

The rate-determining step in the reduction process on the Ru_3Sn_7 (111) catalyst surface is the first dehydroxylation step of CH_3COOH*. In contrast, in the same reaction carried out on a Ru (0001) surface, the third hydrogenation step is the rate-determining step. In addition, the Ru_3Sn_7 alloy has a lower energy barrier for the rate-determining step (81.0 kJ·mol^{-1} on Ru_3Sn_7 (111) vs 123.5 kJ·mol^{-1} on Ru (0001)). Our calculations suggest that the Ru_3Sn_7 (111) surface has a higher catalytic activity for the hydrogenation reaction than pure Ru, which is consistent with our experimental results.

Table 4. Calculated Bader charges of Ru and Sn atom at the adsorption sites on Ru_3Sn_7 (111) surface with different adsorbed reaction intermediates.

Adsorbates	Charge of Ru	Charge of Sn
Pure Ru_3Sn_7 (111) Surface	- 0.64	+ 0.34
CH_3COOH^*	- 0.57	+ 0.40
CH_3CO^*+OH^*	- 0.43	+ 0.67
CH_3CO^*+H^*	- 0.42	+ 0.64
CH_3CHO^*	- 0.38	+ 0.41
CH_3CHO^*+H^*	- 0.37	+ 0.39
$CH_3CH_2O^*$	- 0.30	+ 0.36
$CH_3CH_2O^*$+H^*	- 0.32	+ 0.36
$CH_3CH_2OH^*$	- 0.47	+ 0.34

To explore the better catalytic capability of Ru_3Sn_7 (111) surface, the Bader electron analysis calculations on the stable adsorption structures of different reaction intermediates were carried out (Table 4 and Fig. 11). As shown in Table 4, the calculation results suggest that, in the whole reaction, the Ru site maintains negative charges ranging from -0.30 |e| to -0.57 |e| while the Sn site keeps positive charges ranging from +0.34 |e| to +0.67 |e|. Considering the electrostatic interactions between the reaction intermediates and the surface active sites on the Ru_3Sn_7 (111) surface, the negatively charged Ru site can help facilitating the adsorption of H* species on Ru atom, reducing the adsorption strength of CH_3CH_2O* species and thus lowing the barrier of the hydrogenation of CH_3CH_2O*, while the positively charged Sn site is propitious to the adsorption of CH_3COOH molecule and helps stabilizing the O-containing intermediates. The significant electron transfer can also be confirmed from the charge density difference (CDD) plots of different adsorption intermediates (CH_3CO*, CH_3CHO*, CH_3CH_2O* and CH_3CH_2OH*) on Ru_3Sn_7 (111) surface as shown in Fig. 11. For example, the CDD plot of co-adsorbed CH_3CO* and OH* species (Fig. 11a) shows the electrons transfer from the Sn atoms to the O atoms of the adsorbates and from the Ru atom to the α-C atom of CH_3CO* species. These results indicate the bonding relationships of Sn-O and Ru-α-C and suggest that the surface Sn atoms also take part in the catalytic reaction by acting as a kind of surface catalytic sites rather than just being a structure component. The Ru center bonded with α-C of CH_3CO* and hydrogenated of such intermediate with the dissociated H* to final alcohol with three steps of H* addition.

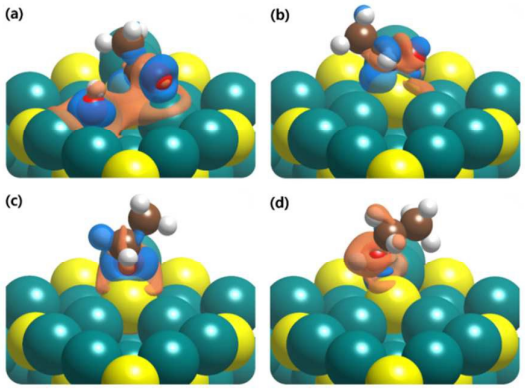

Fig. 11. The charge density difference plots of different adsorbed reaction intermediates on Ru_3Sn_7 (111) surface: (a) CH_3CO*+OH*, (b) CH_3CHO*, (c) CH_3CH_2O* and (d) CH_3CH_2OH*. The blue isosurface corresponds to charge gains and orange isosurface corresponds to the charge lost. Color scheme: yellow: Ru; cyan: Sn, grey: C, red: O, and white: H.

3. Experimental Section

Synthesis of the supported metal catalysts

View Article Online
DOI: 10.1039/C8CY00037A

The metal catalysts supported on SiO_2 were prepared by incipient wetness impregnation. The metal precursor was firstly dissolved in H_2O to afford a solution. Then aqueous was slowly dropped onto SiO_2, and kept continuous stirring at ambient temperature overnight. Afterwards, the as-formed catalysts were filtered, dried at 80 °C overnight. Finally, it was calcined in flowing air (flowing rate: 100 mL·min^{-1}) at 350-460 °C for 4 h, and reduced in flowing hydrogen (flowing rate: 100 mL·min^{-1}) at 250-600 °C for 4 h.

Catalyst characterization

The specific surface area and pore size distribution were performed by N_2 adsorption at 77 K on a BELSORP-MAX instrument after activating the samples under vacuum at 573 K for 10 h. Powder X-ray diffraction (XRD) patterns were measured on Rigaku Ultima IV X-ray diffractometer utilizing Cu-Kα radiation (λ = 1.5405 Å) operated at 35 kV and 25 mA. Scanning electron microscopy (SEM) equipped with energy dispersive X-ray (EDX) analysis unit (Oxford, UK) was operated on a Hitachi S-4800 microscope to illuminate crystal morphology and size. Transmission electron microscopy (TEM) images were performed on a FEI Tecnai G2 F30 microscope working at 300 kV.

X-ray photoelectron spectroscopy (XPS) were performed with Al Kα (hν = 1486.6 eV) radiation on a Thermo Scientific K-Alpha spectrometer. Charging effects were corrected by using the C 1s peak due to adventitious carbon with EB fixed at 284.8 eV.

The temperature programmed reduction (TPR) analysis of calcined catalysts was performed by using Micromeritics tp5080 apparatus equipped with a thermal conductor detector (TCD), using a 5% H_2/He mixture (flowing rate: 20 mL·min^{-1}) and a heating rate of 5 K·min^{-1}.

The IR spectra of adsorbed CO were measured on a Nicolet Fourier transform infrared spectrometer (NEXUS 670). The samples were activated in H_2 at 673 K for 1 h, and then H_2 was removed by Vacuum pump. After the temperature was cooled to 313 K, the samples were exposed to CO until adsorption saturation. Subsequently the samples were evacuated at 313 K to remove the physically adsorbed CO. Afterwards, the IR spectra of adsorbed CO were recorded until no further changes in the spectra were observed.

Catalytic tests

We performed the experiments for conversion of stearic acid and coconut oil as follows: firstly we added the mixture of stearic acid or coconut oil (1.0 g) and catalyst (0.2 g) and the solvent of dodecane (80 mL) into a Parr autoclave (300 ml). Then the autoclave was firstly purged with N_2 to remove the residual air, and in a next step the reaction gas H_2 (4 MPa) was introduced into the Parr reactor at ambient temperature. The reaction was carried out at 240 °C at a stirring speed of 600 rpm. For the kinetic study, the liquid products were collected by *in situ* sampling every 30 min., and then analyzed by a Shimadzu GC coupled with GC-MS.

4. Conclusions

With respect to the promising hydrotreating catalyst, the earlier reports considered that Ru…O=Sn (Ru electronically interacts with Sn oxides) was the active site for fatty acid and fatty ester hydrogenation, but here in this contribution we found that Ru_3Sn_7 nanoclusters as the active catalytic species. The interaction between $Sn^{\delta+}$ and Ru^0 species were not found because of the unchanged BE vaules of $Sn^{\delta+}$ in XPS spectra, suggesting that SnO_x may exist as the isolated species. However, the formation of Ru_3Sn_7 alloy nanoclusters led to an obvious BE shift at Ru^0 and Sn^0 XPS spectra. Our catalytic tests confirmed that the optimal Sn/Ru ratio during preparation of the catalyst achieving the highest fatty alcohol yield was 7/3. The most abundant Ru_3Sn_7 nanoclusters reached the highest rate of 2.45 g·g^{-1}·h^{-1}, while avoiding ester formation at a rate of 0.31 g·g^{-1}·h^{-1} on catalysts formed with a Sn/Ru ratio > 7/3 due to the presence of SnO_2/SiO_2 species. To control the nature of the active species during preparation of the catalyst, the higher reduction temperature at around 460°C suppressed Sn/SiO_2 formation, while Sn/SiO_2 would catalyze the formation of by-product ester at a rate of 0.88 g·g^{-1}·h^{-1}. Thus, supported Ru-Sn bimetallic catalyst consisting of Ru_3Sn_7 nanoclusters as the active sites, was highly active to hydrogenate of C_{12}-C_{18} fatty acids and coconut oil to the corresponding fatty alcohols in near quantitative conversion in a non-polar solvent and under moderate conditions (240°C, 4 MPa H_2).

Density functional theory (DFT) calculations showed the rate-determining step in the reduction process on the Ru_3Sn_7 (111) catalyst surface was the first dehydroxylation step of CH_3COOH*, and by comparison, the third hydrogenation step was the rate-determining step on a Ru (0001) surface. In accordance with our experimental results, the Ru_3Sn_7 alloy showed a lower energy barrier for the rate-determining step (81.0 kJ·mol^{-1} on Ru_3Sn_7 (111) vs 123.5 kJ·mol^{-1} on Ru (0001)). In addition, the CDD plot of *co*-adsorbed CH_3CO* and OH* species demonstrated the electrons transferred from the Sn atoms to the O atoms of the adsorbates and from the Ru atom to the *α*-C atom of CH_3CO* species (bonding relationships of Sn-O and Ru-C). This suggested that the surface Sn atoms took part in the catalytic reaction as a surface adsorption sites as well as a Ru_3Sn_7 structure component, while Ru bonded with α-C of CH_3CO* and hydrogenated of such intermediate with the dissociated H* to alcohol products, leading to Ru_3Sn_7 nanoclusters as an excellent hydrogenation catalysts for converting of esters and acids.

Acknowledgements

This research was supported by National Natural Science Foundation of China (Grant Nos. 21573075, 21373098), the National Key Research and Development Program of China (Grant No. 2016YFB0701100), the Recruitment Program of Global Young Experts in China, and the Shanghai Pujiang Program (Grant No. 14PJ1403500). Part of the computational time is supported by the Performance Computing Center of Jilin Province.

View Article Online
DOI: 10.1039/C8CY00037A

Notes and references

1 J. Pritchard, G. A. Filonenko, R. van Putten, E. J. M. Hensen , E. A. Pidko, *Chem. Soc. Rev.* 2015, **44**, 3808-3833.
2 G. Chelucci, S. Baldino and W. Baratta, *Acc. Chem. Res.* 2015, **48**, 363-379.
3 B. Ma, J. Hu, Y. Wang, C. Zhao,*Green Chem.* 2015, **17**, 4610-4617.
4 B. Ma, C. Zhao, *Green Chem.* 2015, **17**, 1692-1701.
5 B. Ma, X. Yi, L. Chen, A. Zheng, C. Zhao, *J. Mater. Chem. A* 2016, **4**, 11330-11341.
6 J. Zhang, C. Zhao, *ACS Catal.* 2016, **6**, 4512-4525
7 J. Zhang, C. Zhao, *Chem. Commun.* 2015, **51**, 17249-17252.
8 B. Ma, H. Cui, D. Wang, P. Wu, C. Zhao, *Nanoscale* 2017, **9**, 5986-5995.
9 Y. Luo, Comprehensive Handbook of Chemical Bond Energies, CRC Press, London, 2007
10 D. Spasyuk, S. Smith, D. G. Gusev, *Angew. Chem. Int. Ed.* 2012, **51**, 2772-2775.
11 T. V. Stein, M. Meuresch, D. Limper, M. Schmitz, M. Holscher, J. Coetzee, D. J. Cole-Hamilton, J. Klankermayer, W. Leitner, *J. Am. Chem. Soc.* 2014, **136**, 13217-13225.
12 P. Dupau, M. L. Tran Do, S. Gaillard, J. L. Renaud, *Angew. Chem. Int. Ed.* 2014, **53**, 13004-13006.
13 S. Werkmeister, K. Junge, B. Wendt, E. Alberico, H. Jiao, W. Baumann, H. Junge, F. Gallou, M. Beller, *Angew. Chem. Int. Ed.* 2014, **53**, 8722-8726.
14 S. Chakraborty, H. Dai, P. Bhattacharya, N. T. Fairweather, M. S. Gibson, J. A. Krause, H. Guan, *J. Am. Chem. Soc.* 2014, **136**, 7869-7872.
15 Y. Hattori, K. Yamamoto, J. Kaita, M. Matsuda, S. *J.* Yamada, *Am. Oil. Chem. Soc.* 2000, **77**, 1283-1288.
16 E .K. Poels, D. S. Brands, *Appl. Catal. A.* 2000, **191**, 83-96.
17 D. S. Brands, G. U-A-Sai, E. K. Poels, A. Bliek, *J. Catal.* 1999, **186**, 169-180.
18 L. Wu, L. Li, B. Li, C. Zhao, *Chem. Commun.* 2017, **53**, 6152-6155.
19 T. Miyake, T. Makino, S. Taniguchi, H. Watanuki, T. Niki, S. Shimizu, Y. Kojima, M. Sano, *Appl. Catal. A.* 2009, **364**, 108-112.
20 S. Koso, H. Watanabe, K. Okumura, Y. Nakagawa, K. Tomishige, *Appl. Catal. B-Enviro.* 2012, **111**, 27-37.
21 (a) M. C Chia, Y. J. Pagan-Torres, D. Hibbitts, Q. Tan, H. N. Pham, A. K. Datye, M. Neurock, R. J. Davis, J. A. Dumesic, *J. Am. Chem. Soc.* 2011, **133**, 12675-12689; (b) J. Pritchard, G. A. Filonenko, R. V. Putten, E. J. M. Hensen, E. A. Pidko, *Chem. Soc. Rev*., 2015, **44**, 3808—3833.
22 (a) M. J. Mendes, O. A. A. Santos, E. Jordão, A. M. Silva, *Appl. Catal. A.* 2001, **217**, 253-262; (b) Z. Z. Qing, L. Z. Hong, L. Bin, G. S. Zhuo, *Appl. Catal. A*. 2006, **302**, 208-214.
23 (a) F. C. A. Figueiredo, E. Jordão, W. A. Carvalho, *Appl. Catal. A.* 2008, **351**, 259-266; (b) S. A. S. Corradini, G. G. Lenzi, M. K. Lenzi, C. M. F. Soares, O. A. A. Santos, *J Non-Cryst Solids*., 2008, **354**, 4865-4870.
24 (a) R. Luque, J. H. Clark, K. Yoshida, P. L. Gai, *Chem. Commun.* 2009, **35**, 5305-5307; (b) D. A. Echeverri, J. M. Marin, G. M. Restrepo, L. A. Rios, *Appl. Catal. A*. 2009, **366**, 342-347.
25 (a) C. Huang, H. Zhang, Y. Zhao, S. Chen, Z. Liu, *J. Colloid Interface Sci.* 2012, **386**, 60-65; (b) M. A. Sánchez, G. C. Torres, V. A. Mazzieri, C. L. Pieck, *J. Chem. Technol. Biotechnol*., 2017, **92**, 27-42.
26 M. A. Sánchez, V. A. Mazzieri, M. Oportus, P. Reyes, C. L. Pieck, *Catal. Today* 2013, **213**, 81-86.
27 R. D. Adams, E. M. Boswell, B. Captain, A. B. Hungria, P. A. Midgley, R. Raja, J. M. Thomas, *Angew. Chem. Int. Ed.* 2007, **46**, 8182-8185.
28 A. M. Silva, O. A. A. Santos, M. J. Mendes, E. Jordão, M. A. Fraga, *Appl. Catal. A.* 2003, **241**, 155-165.
29 M. A. Sánchez, Y. Pouilloux, V. A. Mazzieri, C. L. Pieck, *Appl. Catal. A.* 2013, **467**, 552-558.
30 S. Eckle, Y. Denkwitz, R. J. Behm, *J. Catal.* 2010, **269**, 255-268.
31 S. Y. Chin, C. T. Williams, M. D. Amiridis, *J. Phy. C. B.* 2006, **110**, 871-882.
32 V. M. Deshpande, K. Ramnarayan, C. S. Nnarasimhan, *J. Catal.* 1990, **121**, 165-173.
33 V. M. Deshpande, K. Ramnarayan, C. S. Nnarasimhan, *J. Catal.* 1990, **121**, 174-182.
34 Y. Pouilloux, F. Autin, C. Guimon, J. Barrault, *J. Catal.* 1998, **176**, 215-224.
35 L. Di, S. Yao, S. Song, G. Wu, W. Dai, N. Guan, L. Li, *Appl. Catal. B*, 2017, **201**, 137–149.
36 J. P. Perdew, K. Burke, M. Ernzerhof, *Phys. Rev. Lett.* 1996, **77**, 3865-3868.
37 O. Schwomma, H. Nowotny, A. Wittmann, *Monatsh. Chem.* 1964, **95**, 1538-1543.

View Article Online
DOI: 10.1039/C8CY00037A

Table of Content: